



Longitudinal predictive modeling of tau progression along the structural connectome

Fan Yang^a, Samadrita Roy Chowdhury^a, Heidi I.L. Jacobs^b, Jorge Sepulcre^b, Van J. Wedeen^b, Keith A. Johnson^b, Joyita Dutta^{a,b,*}

^a University of Massachusetts Lowell, Lowell, MA, United States

^b Massachusetts General Hospital and Harvard Medical School, Boston, MA, United States

ARTICLE INFO

Keywords:

Alzheimer's disease
Tau tangles
Positron emission tomography
Structural connectome
Diffusion tensor imaging

ABSTRACT

Tau neurofibrillary tangles, a pathophysiological hallmark of Alzheimer's disease (AD), exhibit a stereotypical spatiotemporal trajectory that is strongly correlated with disease progression and cognitive decline. Personalized prediction of tau progression is, therefore, vital for the early diagnosis and prognosis of AD. Evidence from both animal and human studies is suggestive of tau transmission along the brains preexisting neural connectivity conduits. We present here an analytic graph diffusion framework for individualized predictive modeling of tau progression along the structural connectome. To account for physiological processes that lead to active generation and clearance of tau alongside passive diffusion, our model uses an inhomogenous graph diffusion equation with a source term and provides closed-form solutions to this equation for linear and exponential source functionals. Longitudinal imaging data from two cohorts, the Harvard Aging Brain Study (HABS) and the Alzheimer's Disease Neuroimaging Initiative (ADNI), were used to validate the model. The clinical data used for developing and validating the model include regional tau measures extracted from longitudinal positron emission tomography (PET) scans based on the ¹⁸F-Flortaucipir radiotracer and individual structural connectivity maps computed from diffusion tensor imaging (DTI) by means of tractography and streamline counting. Two-timepoint tau PET scans were used to assess the goodness of model fit. Three-timepoint tau PET scans were used to assess predictive accuracy via comparison of predicted and observed tau measures at the third timepoint. Our results show high consistency between predicted and observed tau and differential tau from region-based analysis. While the prognostic value of this approach needs to be validated in a larger cohort, our preliminary results suggest that our longitudinal predictive model, which offers an *in vivo* macroscopic perspective on tau progression in the brain, is potentially promising as a personalizable predictive framework for AD.

1. Introduction

Alzheimer's disease (AD) is a progressive neurodegenerative disorder which is the most prevalent form of dementia and is a looming public health challenge (Hebert et al., 2013). Extracellular amyloid- β ($A\beta$) plaques and intracellular tau neurofibrillary tangles are two misfolded protein aggregates implicated in AD pathophysiology (Braak and Braak, 1991). These pathological proteins are known to appear in the brain long before the manifestation of clinical and cognitive symptoms and are key to the early diagnosis of AD during its preclinical (asymptomatic) phase (Dubois et al., 2016; Jack et al., 2010; Sperling et al., 2011). Positron emission tomography (PET) radioligands that avidly and selectively bind to misfolded $A\beta$ and tau have enabled 3D visualization and longitudinal quantitation of these proteins and catalyzed *in vivo* investigations on the biological underpinnings of this complex and

heterogeneous disorder (Herholz and Ebmeier, 2011; Jack et al., 2013; Lois et al., 2019; Saint-Aubert et al., 2017). While the mechanistic basis of AD and the precise links between $A\beta$ and tau aggregation remain unclear, key differences have been noted between the natures of these two underlying proteinopathies. Unlike $A\beta$, tau aggregation is strongly correlated with neurodegeneration and cognitive impairment (Bejanin et al., 2017; Donohue et al., 2017; Gordon et al., 2018; Hedden et al., 2013; La Joie et al., 2020; Palmqvist et al., 2017; Strain et al., 2018; Xia et al., 2017). The two proteins exhibit distinct trajectories of spatial spread as the disease progresses. Whereas $A\beta$ travels from the neocortex to the brainstem and cerebellum, tau first appears in the locus coeruleus and the transentorhinal cortex, spreads to the entorhinal cortex and hippocampus, and finally ascends to the neocortex (Cho et al., 2016; Sepulcre et al., 2017). While tau accumulation in the medial temporal lobe

* Corresponding author at: University of Massachusetts Lowell, Lowell, MA, United States.

E-mail address: dutta.joyita@mgh.harvard.edu (J. Dutta).

<https://doi.org/10.1016/j.neuroimage.2021.118126>.

Received 9 December 2020; Received in revised form 16 April 2021; Accepted 26 April 2021

Available online 4 May 2021.

1053-8119/© 2021 The Author(s). Published by Elsevier Inc. This is an open access article under the CC BY-NC-ND license

(<http://creativecommons.org/licenses/by-nc-nd/4.0/>)

(MTL) is recognized as a feature of normal aging, its spread outside the MTL in conjunction with elevated $A\beta$ is thought to mark the transition from the asymptomatic to the symptomatic phase of AD and the onset of cognitive impairment (Sperling et al., 2014). Methods to model and predict the spatiotemporal spread of tau are, therefore, vital for the early diagnosis and prognosis of AD.

The spatiotemporal propagation pattern of tau lies at the heart of the seminal Braak staging scheme for AD (Braak and Braak, 1991). Recent studies using the PET radiotracer ^{18}F -Flortaucipir have successfully recapitulated histopathological Braak staging in vivo both cross-sectionally (Johnson et al., 2016; Marquie et al., 2017; Ossenkoppele et al., 2016; Scholl et al., 2016; Schwarz et al., 2018; 2016) and longitudinally (Hanseeuw et al., 2019; Harrison et al., 2019; Jack et al., 2018b). The stereotypic spatial topography and temporal trajectory of tau have led to the idea that tau may spread from cell to cell via anatomical or synaptic connectivity in a prion-like fashion (Frost and Diamond, 2010; Lee et al., 2010; Nussbaum et al., 2012; 2013). Initial evidence for this hypothesis emerged from animal models (Ahmed et al., 2014; Boluda et al., 2015; de Calignon et al., 2012). In vivo imaging studies in humans using ^{18}F -Flortaucipir PET have lent further support to this idea by demonstrating strong region-specific associations between regional mean or covariance measures derived from tau PET and localized measures of structural (Jacobs et al., 2018) or functional (Adams et al., 2019; Franzmeier et al., 2020; 2019) connectivity. Graph theory metrics have been used to investigate the temporal directionality in longitudinal $A\beta$ and tau datasets (Sepulcre et al., 2008). Building on seminal work on network diffusion models (NDMs) for neuropathological spread (Raj et al., 2012; 2015), we published, as part of our prior work, a proof of concept of structural connectivity dependent tau spread using human ^{18}F -Flortaucipir PET and diffusion tensor imaging (DTI) data from the Harvard Aging Brain Study (Yang et al., 2019). Very recently, a landmark paper featuring an epidemic spread model (ESM) for tau provided rigorous clinical validation of a connectivity-based approach for tau prediction (Vogel et al., 2020). Underlying both NDM and ESM is the idea of propagation of pathophysiological entities along the brains preexisting, stereotyped neural connectivity conduits captured mathematically by a graph Laplacian matrix (in NDMs) or an equivalent anatomical connection probability matrix (in ESMs). Compared to the ESM (Iturria-Medina et al., 2014), which is a probabilistic model, the NDM (Hu et al., 2016; Raj et al., 2012; 2015) takes an analytic and deterministic approach based on graph-domain partial differential equations (PDEs) and, therefore, is more intuitive and computationally efficient. Existing literature on NDMs, however, is based either on PDEs that are homogeneous (source-free) and rely on passive diffusion or on PDEs with impulse sources sporadically distributed in time. While these frameworks provide qualitative explanations for disease spread and enable source inference, they are less suitable for modeling the simultaneous accretion and propagation of tau for quantitative prediction. Here, we use an analytic graph diffusion approach to quantitatively model the aggregation and propagation of tau along the structural network of the brain.

While passive diffusion from localized sources can qualitatively characterize the spread of misfolded proteins or surrogate measures like atrophy (Hu et al., 2016; Torok et al., 2018), spatiotemporal impulses do not capture the continuous proteopathic seeding processes that underlie tau aggregation (Holmes et al., 2014; Kaufman et al., 2018). Tau molecular seeds are thought to be monomeric or oligomeric forms of the protein that recruit monomeric tau and facilitate misfolding (Shafiei et al., 2017). Recent histological data suggest high expression of seed proteins in the entorhinal cortex, some downstream sites along the Braak pathway, and some white matter tracts (DeVos et al., 2018). New studies have also emphasized the role of $A\beta$ in potentiating the seeding processes that lead to misfolding (Bassil et al., 2020; He et al., 2018). Evi-

dence from cell lines suggests a sigmoidal evolution of tau seeding featuring an exponential growth phase (Holmes et al., 2014). Concomitantly with seeding that leads to misfolded tau accretion, tau clearance is mediated by a combination of proteasomal and autophagic degradative processes (Hyttinen et al., 2014; Lee et al., 2013) with increased emphasis being placed on peripheral pathways and the glymphatic system (Hauglund et al., 2020; Woo et al., 2020). While the exact mechanisms of tau clearance remain an active area of research, they are a key therapeutic target for tauopathies (de Leon and Blennow, 2018). Clearance mechanisms have been previously incorporated in spread models for misfolded proteins (Garbarino and Lorenzi, 2019; Iturria-Medina et al., 2014). To accommodate the cumulative effects of tau seeding and removal, our model is based on an inhomogeneous PDE that includes a source term capturing local trends of active generation and clearance alongside passive diffusion along the structural network of the brain.

In this work, we use regional tau measures derived from longitudinal ^{18}F -Flortaucipir tau PET data collected at two and three timepoints as part of the Harvard Aging Brain Study (Dagley et al., 2017; Johnson et al., 2016). We perform additional validation on three-timepoint ^{18}F -Flortaucipir tau PET scans from the Alzheimer's Disease Neuroimaging Initiative database. Unlike previous works that have modeled misfolded protein dynamics starting from one or more focal point sources and tested the goodness of fit using single-timepoint observations, we model tau seeding and clearance as a continuous-time process and quantitatively validate our model predictions using ^{18}F -Flortaucipir PET measures at a future timepoint. Instead of a population-level healthy structural or functional connectome as used in most prior studies on neuropathological spread, we use structural connectivity information extracted from individual diffusion-weighted magnetic resonance imaging (MRI) scans. Our model allows us to separate passive diffusion trends from active generation/clearance trends for each anatomical region-of-interest (ROI). In Section 2, we derive closed-form analytic solutions for two inhomogeneous graph diffusion PDEs both based on continuous-time source functionals – one linear in time and another exponential. We then present data acquisition and processing details. Our main findings are reported in Section 3. We demonstrate model fitting using two-timepoint data and validate the model in three-timepoint datasets. Finally, in Sections 4 and 5, we summarize this work, discuss its strengths and limitations, and present our envisioned future directions.

2. Methods

2.1. Theory

The spread of a physiological variable can be modeled as a diffusion process along the brain's structural connectome using a graph diffusion equation. The network underlying the diffusion process is defined as a graph $\mathcal{G} = (\mathcal{V}, \mathcal{E})$ where the i th node, $v_i \in \mathcal{V}$, represents the i th gray matter parcellation or anatomical ROI, $|\mathcal{V}| = N$ is the number of ROIs, and $\epsilon_{ij} \in \mathcal{E}$ represents the connectivity strength between node v_i and node v_j . To model the spread of pathological tau species along the brain's structural network, we represent the regional tau burden as a time-varying graph signal vector $\mathbf{x}(t) = [x(v_i, t), v_i \in \mathcal{V}]$, $\mathbf{x}(t) \in \mathbb{R}^N$, where t is a scalar time variable. $\mathbf{x}(t)$ is the solution to a first-order PDE, usually referred to as the network diffusion equation:

$$\frac{\partial \mathbf{x}(t)}{\partial t} = -\beta \mathbf{L} \mathbf{x}(t), \quad (1)$$

where $\mathbf{L} \in \mathbb{R}^{N \times N}$ is the normalized graph Laplacian matrix. Solutions to the homogeneous PDE shown in (1) are of the form:

$$\mathbf{x}(t) = e^{-\beta \mathbf{L}(t-t_0)} \mathbf{x}(t_0), \quad (2)$$

where $\mathbf{x}(t_0)$ is the initial tau burden at time t_0 . To model active generation or clearance alongside passive spread, a source term, $s(t)$, can be

added to (1) leading to an inhomogeneous PDE:

$$\frac{\partial \mathbf{x}(t)}{\partial t} = -\beta \mathbf{L} \mathbf{x}(t) + s(t). \quad (3)$$

Analytic graph diffusion models have evolved from purely qualitative models based on passive diffusion (Raj et al., 2012) to those that incorporate impulse sources of brain atrophy (Hu et al., 2016; Kim et al., 2019). While past work on NDMs has reported high correlations between observed atrophy and predicted atrophy based on inferred point sources earlier in time, quantitative predictions using serialized measures entails modeling of seeding and clearance processes between timepoints. The first model tested here assumes a spatially heterogeneous source linearly varying in time. Building on empirical evidence that tau seeding is a sigmoidal process with an exponential phase after an initial lag, the second model is based on an exponential source term. For both models, the solution to (3) can be computed as a sum of the solution to the homogeneous counterpart and an integral that is derived from the source term as follows:

$$\mathbf{x}(t) = e^{-\beta \mathbf{L}(t-t_0)} \mathbf{x}(t_0) + e^{-\beta \mathbf{L}t} \int_{t_0}^t e^{\beta \mathbf{L}\tau} s(\tau) d\tau. \quad (4)$$

2.1.1. Linear source model

The first model assumes that tau model production and clearance follow a spatially heterogeneous and temporally linear source term $s(t)$ formulated as:

$$s(t) = \mathbf{r}t. \quad (5)$$

Here $\mathbf{r} \in \mathbb{R}^N$ is a linear rate vector. The corresponding PDE is given by:

$$\frac{\partial \mathbf{x}(t)}{\partial t} = -\beta \mathbf{L} \mathbf{x}(t) + \mathbf{r}t. \quad (6)$$

The integrand in (4) for the source term in (5) is:

$$\int_{t_0}^t e^{\beta \mathbf{L}\tau} \mathbf{r}\tau d\tau = \left(\int_{t_0}^t e^{\beta \mathbf{L}\tau} \tau d\tau \right) \mathbf{r} = \frac{1}{\beta} \mathbf{L}^{-1} \left(\int_{t_0}^t (\beta \mathbf{L}) e^{\beta \mathbf{L}\tau} \tau d\tau \right) \mathbf{r} \quad (7)$$

Using the matrix integration by parts formula, we get the following solution to the inhomogeneous PDE in (6):

$$\mathbf{x}(t) = e^{-\beta \mathbf{L}(t-t_0)} \mathbf{x}(t_0) + e^{-\beta \mathbf{L}t} \frac{1}{\beta} \mathbf{L}^{-1} \left(e^{\beta \mathbf{L}t} t - e^{\beta \mathbf{L}t_0} t_0 - \frac{1}{\beta} \mathbf{L}^{-1} (e^{\beta \mathbf{L}t} - e^{\beta \mathbf{L}t_0}) \right) \mathbf{r}. \quad (8)$$

We use the eigenvalue decomposition of the Laplacian, $\mathbf{L} = \mathbf{Q}\mathbf{\Lambda}\mathbf{Q}^{-1}$ and utilize special properties of products of matrix exponentials to simplify the terms as follows:

$$\mathbf{x}(t) = e^{-\beta \mathbf{L}(t-t_0)} \mathbf{x}(t_0) + \frac{1}{\beta} (t\mathbf{L}^{-1} - t_0\mathbf{L}^{-1} e^{-\beta \mathbf{L}(t-t_0)}) \mathbf{r} - \frac{1}{\beta^2} \mathbf{L}^{-2} (\mathbf{I} - e^{-\beta \mathbf{L}(t-t_0)}) \mathbf{r}. \quad (9)$$

The time gap between two sequential PET scans in the HABS cohort is about 2 years. Accounting for the slow pace of tau accumulation in this time frame, we linearize this equation to obtain:

$$\mathbf{x}(t) \approx (\mathbf{I} - \beta \mathbf{L} \Delta t) \mathbf{x}(t_0) + t_0 \Delta t \mathbf{r}. \quad (10)$$

where $\Delta t = t - t_0$ and $\mathbf{I} \in \mathbb{R}^{N \times N}$ is the identity matrix. The inter-scan time, Δt , is a known entity for each individual. To fit the resultant model to a two-timepoint dataset, we solve for the model parameters β and \mathbf{r} by minimizing the following cost function:

$$\Phi_{\text{LIN}}(\beta, \mathbf{r}) = \frac{1}{2} \| \mathbf{f}(\mathbf{x}_0, \beta, \mathbf{r}) - \mathbf{x}_t \|_2^2, \quad (11)$$

where we denote $\mathbf{x}(t_0)$ as \mathbf{x}_0 and $\mathbf{x}(t)$ as \mathbf{x}_t and summarize the model as a function $\mathbf{f}(\mathbf{x}_0, \beta, \mathbf{r})$ of the unknown parameters. We adopt a gradient descent strategy to solve the optimization problem. The gradient derivation is provided in the appendix. To ensure that we have reached the global minimum, we use a multi-start approach with random initializations.

2.1.2. Exponential source model

The second model seeks to emulate an exponential seeding profile by defining a source term featuring a global parameter σ governing the rate of production/clearance and a spatially heterogeneous entity $\alpha \in \mathbb{R}^N$, which captures production or clearance of tau at different ROIs. The resultant source term is formulated as:

$$s(t) = \alpha(e^{\sigma t} - 1), \quad (12)$$

The corresponding PDE is given by:

$$\frac{\partial \mathbf{x}(t)}{\partial t} = -\beta \mathbf{L} \mathbf{x}(t) + \alpha(e^{\sigma t} - 1). \quad (13)$$

We computed the solution to this equation in closed form from (4) and (12) as:

$$\mathbf{x}(t) = e^{-\beta \mathbf{L}(t-t_0)} \mathbf{x}(t_0) + (\sigma \mathbf{I} + \beta \mathbf{L})^{-1} [e^{\sigma t} - e^{\beta \mathbf{L}(t_0-t)} e^{\sigma t_0}] \alpha - (\beta \mathbf{L})^{-1} (\mathbf{I} - e^{\beta \mathbf{L}(t_0-t)}) \alpha. \quad (14)$$

As with the linear source model, given the proximity of serial scans, we approximate this model and express it in terms of $\Delta t = t - t_0$ as follows:

$$\mathbf{x}(t) \approx (\mathbf{I} - \beta \mathbf{L} \Delta t) \mathbf{x}(t_0) + (\sigma \mathbf{I} + \beta \mathbf{L})^{-1} [\sigma \mathbf{I} \Delta t + \beta \mathbf{L} \Delta t (\mathbf{I} + \sigma \mathbf{I} t_0)] \alpha - \mathbf{I} \Delta t \alpha. \quad (15)$$

To fit this model to a two-timepoint dataset, we solve for the model parameters β , α , and \mathbf{r} by minimizing the following cost function:

$$\Phi_{\text{EXP}}(\beta, \alpha, \sigma) = \frac{1}{2} \| \mathbf{f}(\mathbf{x}_0, \beta, \alpha, \sigma) - \mathbf{x}_t \|_2^2, \quad (16)$$

where we denote $\mathbf{x}(t_0)$ as \mathbf{x}_0 and $\mathbf{x}(t)$ as \mathbf{x}_t and summarize the model as a function $\mathbf{f}(\mathbf{x}_0, \beta, \alpha, \sigma)$ of the unknown parameters. Once again, we use gradient descent to minimize the cost function. The gradient derivation is provided in the appendix. We used a multi-start approach with random initializations to attain global minima.

2.2. Data description

2.2.1. Participants

The overall workflow is summarized in Fig. 1. Our model validation relies on two independent data sources: the Harvard Aging Brain Study (HABS) and the Alzheimer's Disease Neuroimaging Initiative (ADNI). We use longitudinal structural MRI, diffusion MRI, and ^{18}F -Flortaucipir PET imaging for tau from both repositories. Additionally, for each HABS data sample, we utilize our knowledge of each individual's $A\beta$ -status derived from ^{11}C -Pittsburgh Compound-B (PiB) PET imaging.

HABS is an ongoing longitudinal study designed to further our understanding of what differentiates normal aging from preclinical AD. Preclinical AD refers to the presymptomatic stage of AD which is usually tracked using pathophysiological biomarkers, e.g., $A\beta$ and tau measures from PET or cerebrospinal fluid (Jack et al., 2018a). HABS participants who underwent 3T diffusion-weighted MRI scans at baseline and subsequently underwent serial ^{18}F -Flortaucipir PET scans at two or three timepoints were included in our data analysis. All participants were cognitively normal (CN) elderly individuals. Of the $n = 68$ HABS participants used in this work, 59 had only two ^{18}F -Flortaucipir scans (baseline and follow-up), while the remaining nine had a third ^{18}F -Flortaucipir scan (baseline and two follow-ups). Henceforth, we will refer to these two subsets as the HABS-2TP (two-timepoint) and HABS-3TP (three-timepoint) datasets respectively. The HABS-2TP dataset is used for parameter computation and assessing the goodness of model fitting while the HABS-3TP dataset is utilized for validation of downstream prediction of tau.

ADNI is a multisite study that features serial collection of neuroimaging, neuropsychological, biochemical, genetic, and other measures from cognitively normal and impaired human subjects (<http://adni.loni.usc.edu/>). In our work, we use data from $n = 22$ ADNI3 participants who underwent 3T MRI and ^{18}F -Flortaucipir PET scans at baseline and subsequently underwent serial MRI and ^{18}F -Flortaucipir

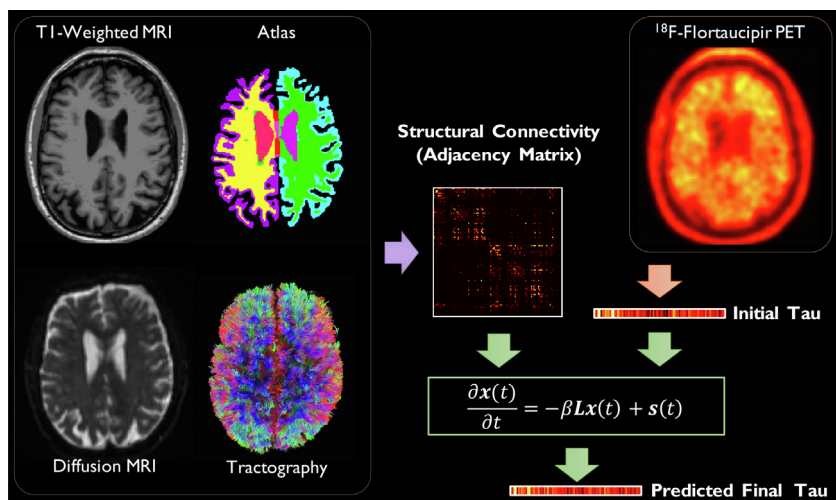


Fig. 1. Overall workflow showing sample images: T1-weighted MRI, the warped anatomical atlas, diffusion MRI, white matter fiber tracts, and ^{18}F -Flortaucipir PET. The atlas is generated from FreeSurfer parcellation of the T1-weighted MR image. White matter fiber tracts are reconstructed from diffusion MRI via tractography. Fiber counting is performed on the segmented diffusion image volumes to derive pairwise inter-ROI connection strengths thereby yielding a graph adjacency matrix, from which a weighted Laplacian is computed. ROI means from ^{18}F -Flortaucipir PET constitute the initial regional tau burden at baseline and are represented as a graph signal vector. The predicted final tau at follow-up is computed by solving an inhomogeneous PDE.

Table 1
Participant demographics*.

Dataset	<i>n</i> (female)	Age (yrs.)	$\Delta t_{\text{DTI-PET}}$ (yrs.)	MMSE	CDR	PiB FLR
HABS-2TP	59 (35)	76.07 \pm 6.22	2.27 \pm 1.03	29.29 \pm 1.05	0 \pm 0.07	1.48 \pm 0.50
HABS-3TP	9 (1)	74.19 \pm 5.08	2.37 \pm 0.46	28.67 \pm 1.58	0 \pm 0	1.48 \pm 0.28
ADNI-3TP	22 (17)	73.80 \pm 9.55	-0.05 \pm 0.23	27.55 \pm 3.43	0.20 \pm 0.33	N/A

*Values are in the format mean \pm standard deviation.

MMSE, mini-mental state examination; CDR, clinical Dementia rating.

PET scans after 24- and 48-month followup timepoints. 10 of these subjects are elderly CN individuals, 7 had mild cognitive impairment (MCI), and 5 were AD patients. Henceforth, we will refer to this dataset as the ADNI-3TP (three-timepoint) dataset. $A\beta$ PET scans are not available for all subjects in the ADNI-3TP dataset. Therefore, we do not consider ADNI $A\beta$ -status in our analysis.

Table 1 presents a summary of participant demographics. The time gap between the DTI scan and the baseline ^{18}F -Flortaucipir PET is indicated as $\Delta t_{\text{DTI-PET}}$. HABS uses the average PiB distribution volume ratio in frontal, lateral temporoparietal, and retrosplenial (FLR) ROIs for $A\beta$ quantitation. This measure is reported in the “PiB FLR” column.

2.2.2. Data acquisition

For the HABS dataset, all MRI scanning was performed on a Siemens Tim Trio 3T imaging system with a 12-channel phased-array head coil. T1-weighted scans were based on a Magnetization Prepared Rapid Gradient-Echo (MPRAGE) sequence with a voxel size of $1.05 \times 1.05 \times 1.2 \text{ mm}^3$. The diffusion-weighted scans were acquired using a spin-echo echo-planar imaging sequence: echo time (TE) 84 ms, repetition time (TR) 8040 ms, field-of-view (FOV) $256 \times 256 \times 128$, voxel size 2 mm isotropic with 30 isotropically distributed orientations for the diffusion-sensitizing gradients at a b -value of 700 s/mm^2 . PET scans were performed on a Siemens ECAT PET HR+ scanner (3D mode, 63 image planes, 15.2 cm axial FOV, 5.6 mm transaxial resolution, and 2.4 mm slice interval). For PiB PET scans, an 8.5–15 mCi bolus injection was immediately followed by a 60-minute dynamic acquisition. ^{18}F -Flortaucipir PET data were acquired for the 80 to 1005 min time window following a $10 \pm 1 \text{ mCi}$ bolus injection. Serial tau PET imaging was conducted with intervals of 25.5 ± 8.4 months between consecutive scans.

For the ADNI dataset, all MRI data was obtained on Siemens Prisma 3T scanners. T1-weighted anatomical scans were based on an MPRAGE sequence with voxel size $1 \times 1 \times 1 \text{ mm}^3$, FOV $208 \times 240 \times 256$, TE 3 ms, TR 2,300 ms, and inversion time (TI) 900 ms. The diffusion-weighted scans were acquired with TE 56 ms, TR 7,200 ms, FOV $232 \times 232 \times 160$, voxel size 2 mm, and diffusion-sensitizing gradients at a b -value of

1000 s/mm^2 . ^{18}F -Flortaucipir PET data were acquired for the 75 to 1055 min time window following a $10 \pm 1 \text{ mCi}$ bolus injection. Serial tau PET imaging was conducted with intervals of 24 months between consecutive scans.

2.3. Data processing

2.3.1. Computation of tau measures

T1-weighted MRI preprocessing was performed using FreeSurfer v6.0 (Dale et al., 1999; Fischl et al., 1999). We utilized the FreeSurfer based auto-reconstruction process that incorporates motion correction, intensity normalization, skull stripping, and linear and nonlinear volumetric registration leading to anatomical (cortical and subcortical) parcellations.

PET images were rigidly coregistered to the T1 MR images using FSL (Jenkinson et al., 2012; Smith et al., 2004; Woolrich et al., 2009). FreeSurfer ROIs defined by MR as described above were transformed into the PET native space. For both HABS and ADNI, standardized uptake value ratios (SUVRs; cerebellar gray matter reference) were computed for ^{18}F -Flortaucipir PET. For HABS PiB PET scans, and distribution volume ratios (DVRs; cerebellar reference) were computed, and $A\beta$ + / status was determined by using a cutoff of 1.20 on the PiB FLR DVR.

85 ROIs were retained from the 112 regions defined by the FreeSurfer Desikan-Killiany atlas after discarding white matter ROIs and ROIs that are known to have high off-target binding. We extracted mean SUVRs for the 85 ROIs to form an 85×1 intensity vector from each ^{18}F -Flortaucipir PET image.

2.3.2. Structural connectome computation

The diffusion MRI scans were preprocessed using FSL to correct discrepancies arising from subject motion, eddy current distortion, and susceptibility. Diffusion tensors were reconstructed using DSI Studio, and deterministic fiber tracking was performed to obtain the streamlines between different brain regions. Whole-brain seeding was used. The termination criterion was decided by fractional anisotropy. An “end in region criterion” was applied to retain only those streamlines that end in an ROI

thereby ensuring that the final set of streamlines are representative of the actual inter-ROI connectivity. We used an angular threshold of 45° , an anisotropy threshold of 0.6 times Otsu's threshold (effective range of 0.14 to 0.45 across the subjects), a total of 50,000 seeds, and a fiber length range of 30 to 300 mm. The fiber trajectories were smoothed by averaging the propagation direction with 40% of the previous direction. We used identical parameter settings for all participants.

The tracts were normalized by length, and only those ending in the 85 retained gray-matter ROIs from the FreeSurfer Desikan-Killiany atlas were considered. The streamlines between each pair of ROIs were counted to generate pairwise inter-ROI connection strengths. Individual 85×85 adjacency matrices were thus created for ROI-based analysis to capture individualized structural connectivity profiles for each human subject. Normalized weighted Laplacian matrices were computed from the adjacency matrices.

2.3.3. Model implementation and validation

Model parameters for both the linear and exponential source models were fitted by minimizing the cost functions in (11) and (16) respectively. The cost functions were iteratively minimized using an alternating gradient strategy with the linear parameters (e.g., the vector parameters α and r) and the nonlinear parameters (e.g., the scalar parameters β and σ) updated in sequential sub-iterations. All gradients were computed analytically as described in the appendix. The HABS-2TP dataset was used to demonstrate model fitting performance. The HABS-3TP and ADNI-3TP datasets were used for independent validation at the third timepoint. For assessment of model fitting in the HABS-2TP dataset and prediction accuracy in the HABS-3TP and ADNI-3TP datasets, we compare predicted and observed SUVRs and differential SUVRs (dSUVRs). We use the normalized root-mean-square error (NRMSE) and the normalized mean absolute error (NMAE) between the observed and predicted SUVRs and dSUVRs as quantitative and objective figures-of-merit to assess model performance. The NRMSE is based on an L_2 norm of the differences between observed and predicted measures, while the NMAE is based on the L_1 norm. While both metrics are quantitative in nature, they penalize larger and smaller errors to different relative extents. Both metrics are, therefore, used for robust assessment of model accuracy.

3. Results

3.1. Goodness of fit in HABS-2TP data

Parameter fitting was done for individual subjects in the HABS-2TP dataset using the linear and exponential source models. Recent literature highlights the predictive value of tracking the longitudinal change in inferior temporal lobe (IFT) tau (Hanseeuw et al., 2019). Accordingly, in our analysis, we separate individuals with more than 1% increase in IFT tau burden from baseline to follow-up (tau \uparrow) from those with no discernible increase (< 1%) in IFT tau burden from baseline to follow-up (tau ∇).

We also separate the subjects based on their $A\beta$ status into $A\beta+$ and $A\beta$ categories. Furthermore, since tau evolution can be conceptualized as a slow-moving process, a high degree of correlation could exist between the two timepoints. Therefore, alongside computing ROI mean SUVRs to assess goodness of fit, we also computed dSUVRs. Fig. 2 depicts observed and predicted mean SUVRs and dSUVRs in 10 ROIs deemed critical for tau in preclinical AD for two representative individuals – a tau \uparrow subject and a tau ∇ subject. These ROIs were selected for visualization based on recent literature that identified several regions in the brain that optimally capture longitudinal change early in the Alzheimers continuum (Jack et al., 2018b; Sanchez et al., 2021). While there is good agreement between observed and predicted SUVRs for both the linear and exponential source models, the latter more robustly estimates dSUVRs. Table 2 shows quantitative metrics for the goodness of fit, namely the NRMSE and NMAE between the observed and predicted SUVRs and dSUVRs for all ROIs. Consistent trends for the two metrics, as observed

here, are indicative of robustness, as the two metrics penalize larger and smaller errors to different extents. The exponential source model led to smaller errors in dSUVRs than the linear model for all subjects and for the tau \uparrow and tau ∇ subgroups. We also separately report performance for $A\beta+$ and $A\beta$ cases. The exponential source model performed better in the tau \uparrow subgroup, which features a greater proportion of signal over noise in the dSUVRs, compared to the tau ∇ subgroup, which exhibits relatively subtle longitudinal changes that are more susceptible to noise-induced variations. The reverse was true for the linear source model. In comparison, there was a smaller difference in the data fidelity metrics between the $A\beta+$ and $A\beta$ groups. This could be explained by the fact that the $A\beta+$ subgroup in our cohort includes many tau ∇ subjects, while the $A\beta$ subgroup includes many tau \uparrow subjects.

3.2. Model interpretation

To facilitate model interpretation, we separately examine the propagative and generative components for the exponential source model. Fig. 3 shows a connectogram summarizing the results of model fitting. The plot uses a circular layout with all fitted ROIs indicated on the outer annulus (Annulus 4). The inter-ROI links in the center offer a population-level snapshot of structural connectivity with the link thickness commensurate with pairwise connection strengths scaled by the reciprocal of the ROI size (scaling done for improved visibility). The critical ROIs highlighted in Fig. 2 and their connectivities are indicated in red. In a graph diffusion model, $-Lx(t)$ is proportional to the rate of aggregation in each ROI purely due to passive diffusion from its connected neighbors. Annulus 1 depicts for each ROI a bar graph of the distribution of $Lx(t)$ across subjects sorted from most negative (inward diffusion or accumulation – yellow) to most positive (outward diffusion or dissipation – green). Based on the sign of the median value of this measure, each ROI can be determined to be either a dissipator or an accumulator. In the exponential source model in (13), the vector α acts as a source/producer or sink/remover depending on its sign and could be linked to the physiological processes of seeding or clearance. Annulus 2 depicts for each ROI a bar graph of the distribution of α across subjects sorted from most negative (remover or sink – blue) to most positive (producer or source – red). Based on the sign of the median value of this measure, each ROI can be determined to be either a source or a sink. All ROIs can be placed into one of four classes depending on its source/sink and accumulator/dissipator status based on medians. This overall classification is indicated in Annulus 4 for four cross-sectional subgroups: (1) Tau ∇ , $A\beta$, $n = 21$, (2) Tau ∇ , $A\beta+$, $n = 11$, (3) Tau \uparrow , $A\beta$, $n = 17$, and (4) Tau \uparrow , $A\beta+$, $n = 10$. This analysis suggests that several of the ROIs critical in early AD switch classes from sink + dissipator to source + dissipator when the tau or $A\beta$ status changes.

Whereas the entorhinal cortex (ERC) and the IFT regions are a source + dissipator in all but the tau ∇ , $A\beta$ subgroup, the hippocampus (HIP) is a source + dissipator only for tau \uparrow cases while the amygdala (AMG) and the parahippocampal gyrus (PHG) are a source + dissipator only for the tau \uparrow , $A\beta+$ subgroup. While these groupings are cross-sectional, the sequence is consistent with a recently reported tau seeding assay suggesting that the HIP and PHG are prominent downstream sites of seeding following the ERC (DeVos et al., 2018). This sequence of seeding sites is also consistent with the Braak pathway. As per the histological evidence underlying Braaks landmark paper (Braak and Braak, 1991), whereas stage I is associated with isolated or low levels of neurofibrillary tangles in the trans-ERC and ERC sub-regions, the new areas recruited in stage II include pyramidal cells in the HIP and the AMG. The connectivity profile in our data also confirms strong ERC-HIP, ERC-PHG, and HIP-AMG connectivity.

3.3. Model validation with HABS-3TP data

To test the models predictive capability of downstream tau aggregation from baseline, we validated the model using the HABS-3TP cohort.

Table 2
Model fitting accuracy in the HABS-2TP dataset.

Metrics	NRMSE				NMAE			
	LIN		EXP		LIN		EXP	
	SUVR	dSUVR	SUVR	dSUVR	SUVR	dSUVR	SUVR	dSUVR
All (59)	0.0370	0.0869	0.0227	0.0532	0.0365	0.0857	0.0147	0.0345
Tau ↑ (27)	0.0412	0.1011	0.0171	0.0421	0.0407	0.0999	0.0106	0.0260
Tau γ (32)	0.0365	0.0859	0.0272	0.0639	0.0360	0.0846	0.0189	0.0444
Aβ+ (21)	0.0391	0.0966	0.0247	0.0612	0.0388	0.0959	0.0149	0.0369
Aβ- (38)	0.0378	0.0998	0.0227	0.0599	0.0372	0.0981	0.0153	0.0404

LIN, linear source model; EXP, exponential source model.

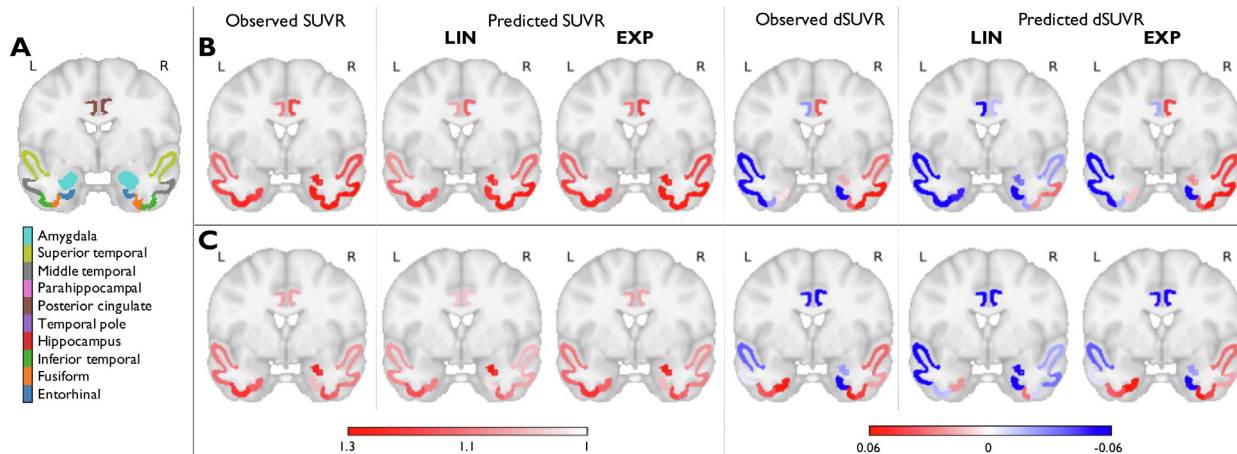


Fig. 2. Fitting results using the linear (LIN) and exponential (EXP) source models in the HABS-2TP dataset. (A) A coronal slice in MNI152 space showing 10 ROIs deemed critical for tau in early AD. The ROIs (based on the FreeSurfer Desikan-Killiany atlas) are overlaid on the MNI template. Observed and predicted ROI mean SUVRs and dSUVRs in (B) A subject with increasing IFT tau between baseline and follow-up and (C) A subject with no significant increase in IFT tau between baseline and follow-up.

Table 3
Prediction accuracy in the HABS-3TP dataset.

Metrics	NRMSE				NMAE			
	LIN		EXP		LIN		EXP	
	SUVR	dSUVR	SUVR	dSUVR	SUVR	dSUVR	SUVR	dSUVR
All (9)	0.1722	0.1804	0.0941	0.0985	0.1217	0.1274	0.0635	0.0665
Tau ↑ (6)	0.1785	0.1869	0.1195	0.1113	0.1287	0.1349	0.0778	0.0725
Tau γ (3)	0.1813	0.4610	0.0644	0.1610	0.1183	0.3009	0.0489	0.1222
Aβ+ (6)	0.1913	0.2004	0.0876	0.0918	0.1418	0.1486	0.0753	0.0789
Aβ- (3)	0.1503	0.3417	0.0633	0.1439	0.0972	0.2210	0.0474	0.1078

LIN, linear source model; EXP, exponential source model.

The model parameters are fitted by utilizing the first two timepoints, while prediction accuracy is assessed at the third timepoint. It should be noted that the parameter fitting step is not allowed access to any data from the third timepoint.

Fig. 4 shows observed and predicted mean SUVRs and dSUVRs in the 10 ROIs that are critical for tau in preclinical AD for two representative individuals – a tau ↑ subject and a tau γ subject from the HABS-3TP cohort. Table 3 presents NRMSE and NMAE between the observed and predicted SUVRs and dSUVRs for all ROIs.

The degradation of performance from the model fitting task to the prediction task is an expected outcome as the third timepoint is not previously seen by the model and also because, in many regions, the differential fitted by the model is dominated by noise. The relative performance of the exponential and linear source models at the prediction task is consistent with the model fitting results.

3.4. Secondary validation with ADNI-3TP data

For additional validation, we tested the predictive capability of our model on the ADNI-3TP dataset. Model fitting and prediction steps sim-

ilar to those performed for HABS were repeated on this cohort. Fig. 5 shows observed and predicted mean SUVRs and dSUVRs in the 10 tau-critical ROIs for two representative individuals – a tau ↑ subject and a tau γ subject from the ADNI-3TP cohort. Table 4 presents NRMSE and NMAE between the observed and predicted SUVRs and dSUVRs for all ROIs. The trends in the ADNI results are consistent with those in HABS results that confirming the overall robustness of the predictive model.

4. Discussion

Motivated by literary evidence that the spatiotemporal trajectory of misfolded tau protein may provide clues to the course of AD, we modeled pathological tau spread via an inhomogeneous PDE. This equation builds on the well-established NDM that portrays tau propagation as a passive diffusion process along conduits determined by the brain's structural network. Though we recognize the role that diffusion plays in modeling the transmission of tau across brain regions, passive diffusion cannot alone explain the escalation in tau burden that is a signature of AD progression. We thus assign to the NDM an additional source term thereby creating an inhomogeneous PDE. We generated closed-form so-

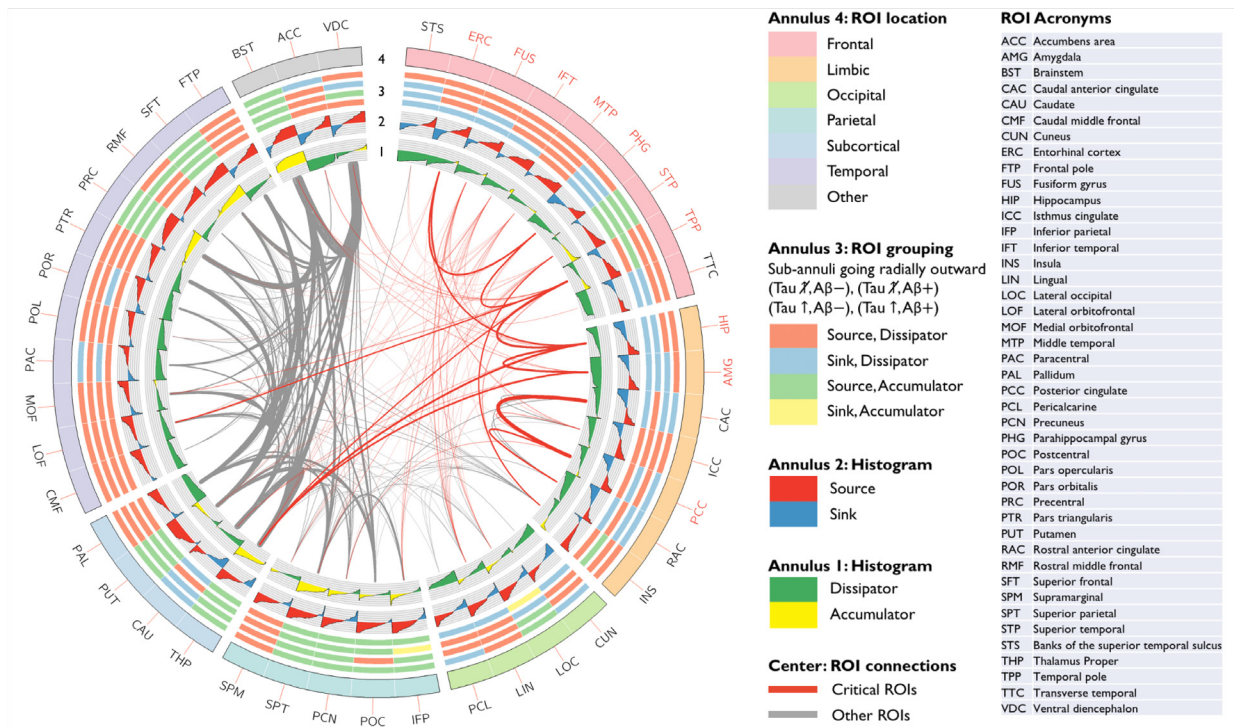


Fig. 3. A connectogram summarizing model-fitting results. All ROIs are indicated on the outer annulus (Annulus 4) and color-coded based on their anatomical location. The inter-ROI links in the center offer a population-level snapshot of structural connectivity with the link thickness commensurate with pairwise connection strengths scaled by the reciprocal of the ROI size (scaling done for improved visibility). All fibers connected to the critical ROIs indicated in Fig. 2 are shown in red. Annulus 1 shows for each ROI a bar graph of the distribution of a diffusion measure across subjects sorted from most negative (inward diffusion or accumulation – yellow) to most positive (outward diffusion or dissipation – green). Annulus 2 shows for each ROI a bar graph of the distribution of the source/sink strength across subjects sorted from most negative (sink/remover – blue) to most positive (source/producer – red). All ROIs can be placed into one of four classes depending on its source/sink and accumulator/dissipator status. Annulus 3 shows this overall classification for four subject groups corresponding to the sub-annuli going radially outward: (τ , γ , $A\beta$), (τ , γ , $A\beta$ +), (τ , γ , $A\beta$), (τ , γ , $A\beta$ +). (For interpretation of the references to color in this figure legend, the reader is referred to the web version of this article.)

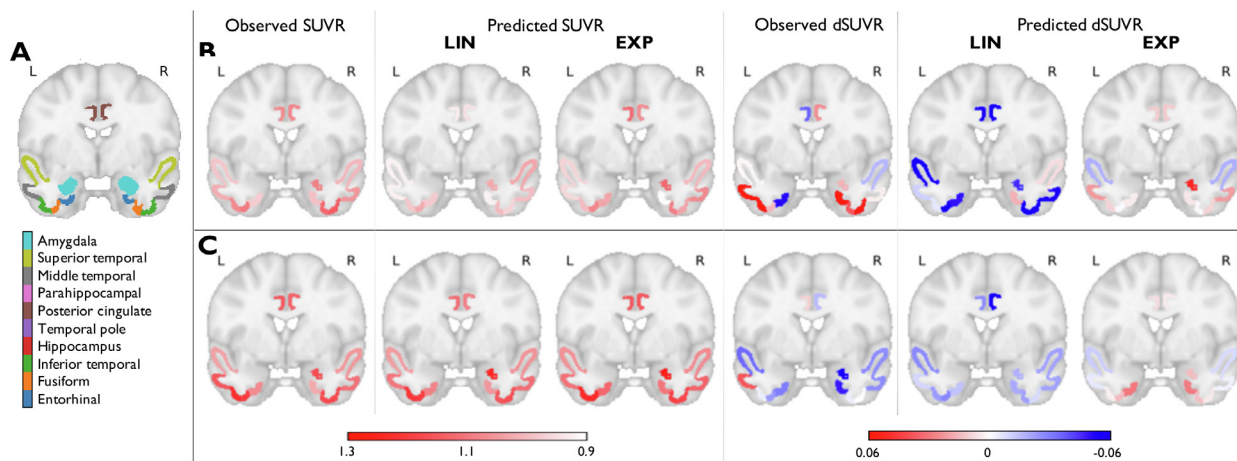


Fig. 4. Prediction results using linear (LIN) and exponential (EXP) source models in the HABS-3TP dataset. (A) A coronal slice in MNI152 space showing 10 ROIs deemed critical for tau in early AD. The ROIs (based on the FreeSurfer Desikan-Killiany atlas) are overlaid on the MNI template. Observed and predicted ROI mean SUVRs and dSUVRs in (B) A subject with increasing IFT tau between baseline and follow-up and (C) A subject with no significant increase in IFT tau between baseline and follow-up.

lutions to this equation for linear and exponential source functionals. The resultant parametric models were fitted by iterative computation of the model parameters using tau PET data at two timepoints. To test the model’s accuracy, we compared predicted and observed tau at a third timepoint. For this comparison, we used ROI mean SUVRs as measures of localized tau burden and additionally used dSUVRs to quantify the change across timepoints. As quantitative figures of merit, we use the

NRMSE and NMAE error measures. The exponential source model outperformed the linear source for all data groupings.

Source modeling allows us to examine the source/sink and accumulator/dissipator status of each ROI based on the medians. Many ROIs considered critical in early AD were classified as sink + dissipator for the tau γ , $A\beta$ subgroup and switched to source + dissipator when the tau or $A\beta$ status changed. The posterior cingulate cortex (PCC) showed

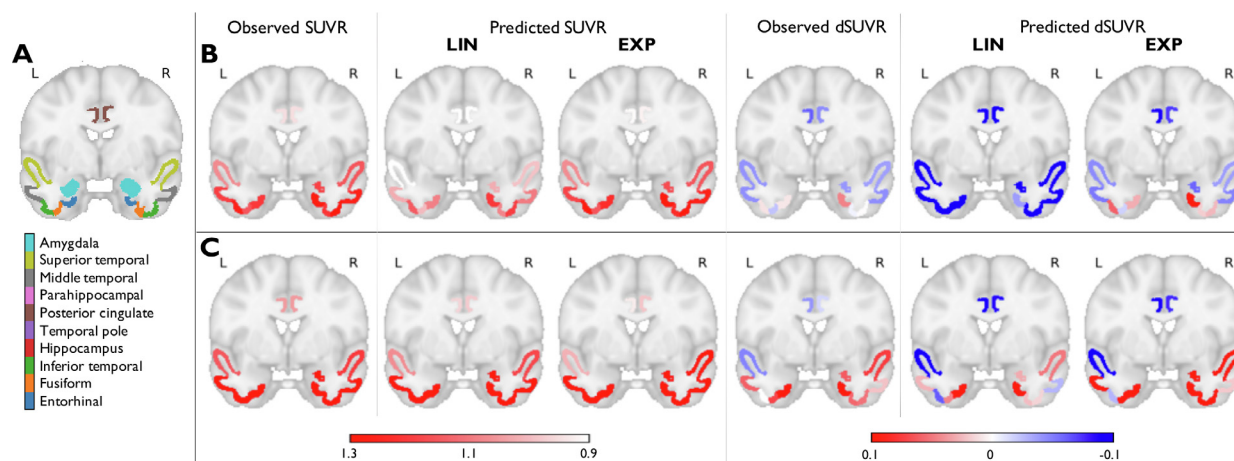


Fig. 5. Prediction results using linear (LIN) and exponential (EXP) source models in the ADNI-3TP dataset. (A) A coronal slice in MNI152 space showing 10 ROIs deemed critical for tau in early AD. The ROIs (based on the FreeSurfer Desikan-Killiany atlas) are overlaid on the MNI template. Observed and predicted ROI mean SUVRs and dSUVRs in (B) A subject with increasing IFT tau between baseline and follow-up and (C) A subject with no significant increase in IFT tau between baseline and follow-up.

Table 4
Prediction accuracy in the ADNI-3TP dataset.

Metrics	NRMSE				NMAE			
	LIN		EXP		LIN		EXP	
Group (n)	SUVR	dSUVR	SUVR	dSUVR	SUVR	dSUVR	SUVR	dSUVR
All (22)	0.0829	0.2754	0.0442	0.1470	0.0724	0.2406	0.0308	0.1023
Tau ↑ (10)	0.1006	0.3883	0.0566	0.2185	0.0889	0.3431	0.0393	0.1515
Tau ↓ (12)	0.0799	0.2341	0.0384	0.1125	0.0712	0.2086	0.0289	0.0847
MCI (7)	0.0672	0.2662	0.0363	0.1438	0.0600	0.2378	0.0270	0.1069
CN (12)	0.1395	0.3697	0.0640	0.1695	0.1230	0.3258	0.0458	0.1214
AD (3)	0.1204	0.3418	0.0871	0.2473	0.1038	0.2949	0.0603	0.1712

LIN, linear source model; EXP, exponential source model.

a reverse transition from source + dissipator to sink + dissipator from the $A\beta$ to the $A\beta +$ subgroups. The latter observation is interesting since prior work in both cross-sectional (Sepulcre et al., 2016) and longitudinal (Jacobs et al., 2018) cohorts suggests the PCC region to be an important site of interaction between $A\beta$ and tau.

A key challenge toward capturing in vivo tau measures using PET is the off-target binding of ^{18}F -Flortaucipir in several ROIs, including the basal ganglia, choroid plexus, and the meninges. At the ROI level, we circumvented this impediment by removing several ROIs that exhibit high off-target binding. As future work, we will address off-target effects enhanced by spillover by partial volume correcting our data via image deblurring (Song et al., 2019) and examine the impact of this on model fitting and prediction. Consistent with the focus of the HABS cohort for preclinical AD, we centered our attention on ROIs that exhibit pathological tau in the early and asymptomatic disease stages. While the subtle but detectable changes in in vivo tau burden in the preclinical stage are of particular significance in the early diagnosis and prognosis of AD, a major challenge is posed by the noise susceptibility of the differential tau PET signals. For more robust interpretation, our future work will involve validation at multiple timepoints, which will be achievable within a few years as more three-timepoint and some four-timepoint datasets become available in the HABS cohort. While, due to the availability of only two timepoints for fitting, we have restricted ourselves to linearized source models, as more timepoints are available, we will be able to investigate fully nonlinear solutions and explore more sophisticated source functionals.

A key limitation of the current study is the small size of our dataset. ^{18}F -Flortaucipir PET is a relatively recent technology, which makes the cohort sizes for serial datasets too small for robust statistical analyses.

But, as more data become available in the HABS and ADNI cohorts, the increased statistical power may be harnessed to more robustly validate longitudinal tau progression models.

Very recent literature suggests the superiority of probabilistic tractography over the deterministic approach used in this paper (Girard et al., 2020). As future work, we will use probabilistic and anatomically corrected tractography to create structural connectomes and compare the relative merits of probabilistic and deterministic tractography in the context of tau progression modeling.

It should be noted that neurodegenerative diseases like AD lead to gradual changes in the structural connectome. Similar to past efforts by other research groups on spread models for neurodegenerative diseases, we consider a static structural connectivity profile in our model. As future research, we will investigate models that accommodate an evolving differential operator.

5. Conclusion

We presented here a model to capture the spatiotemporal evolution of tau and validated it using data from the HABS and ADNI cohorts. By combining PET and DTI, we offered a macroscopic perspective on tau propagation along neural pathways. The structural network of the brain was reconstructed via a tractography-derived connectome while longitudinal tau measures based on ^{18}F -Flortaucipir PET scans were used to capture the temporal evolution of misfolded tau. We performed quantitative assessment of model fitting and prediction accuracy based on both SUVRs and dSUVRs. To our knowledge, this is the first attempt to model tau progression in an individualized manner with model validation performed using longitudinal observations. Our approach is distinct from prior efforts in that it is data-driven and does not start with a (hypotheti-

cal) focal seed. As an analytic model, this approach is more intuitive and computationally efficient than alternative probabilistic models of protein dynamics. Our model lays the groundwork for an analytic framework for personalized prediction of disease progression based on individual (rather than group-level) connectivity graphs. At a preliminary level, our model appears promising as a tool for longitudinal tracking of tau aggregation. Since the model has only been tested for a small number of subjects, studies in larger cohorts need to be performed to assess its full prognostic potential.

Credit authorship contribution statement

Fan Yang: Data curation, Software, Validation, Visualization. **Samadrita Roy Chowdhury:** Methodology, Software, Validation, Writing - original draft, Writing - review & editing, Supervision. **Heidi I.L. Jacobs:** Data curation, Methodology, Writing - review & editing. **Jorge Sepulcre:** Data curation, Methodology, Writing - review & editing. **Van J. Wedeen:** Methodology, Writing - review & editing. **Keith A. Johnson:** Methodology, Writing - review & editing. **Joyita Dutta:** Conceptualization, Methodology, Resources, Writing - original draft, Writing - review & editing, Supervision, Funding acquisition.

Acknowledgments

This work was supported in part by the NIH grants K01AG050711 and R03AG070750.

Appendix A

A1. Gradient computation for the linear source model

Minimization of the cost function in (11) requires the computation of gradients of $f(x_0, \beta, r)$ with respect to β and r . These can be computed as follows:

$$\frac{\partial f}{\partial \beta} = -\Delta t L x_0. \quad (17)$$

$$\nabla_r f = t_0 \Delta t \mathbf{1}. \quad (18)$$

A2. Gradient computation for the exponential source model

Minimization of the cost function in (16) requires the computation of the gradients of $f(x_0, \beta, \alpha, \sigma)$ with respect to β , α , and r . The gradient of the data-fit cost $\Phi_{\text{EXP}}(\beta, \alpha, \sigma)$ with respect to an arbitrary parameter vector $\mathbf{z} \in \mathbb{R}^M$ ($M = 1$ for β and σ , $M = N$ for α) can be computed from the gradient $\nabla_z f$ using:

$$\nabla_z \Phi_{\text{EXP}} = (\nabla_z f)(f - x_t). \quad (19)$$

This would require us to tackle the matrix inverse in (15). To this end, we use the eigenvalue decomposition of the Laplacian given by $L = Q\Lambda Q^{-1}$, where $Q^T = Q^{-1}$ due to the symmetry of L . The matrix inverse term can then be written as:

$$\begin{aligned} \mathbf{M}(\beta, \sigma) &= (\sigma \mathbf{I} + \beta L)^{-1} = [Q(\sigma \mathbf{I} + \beta \Lambda)Q^T + Q(\beta \Lambda)Q^T]^{-1} \\ &= Q[\sigma \mathbf{I} + \beta \Lambda]^{-1}Q^T. \end{aligned} \quad (20)$$

The derivatives of $\mathbf{M}(\beta, \sigma)$ with respect to the unknowns β and σ can be obtained as follows:

$$\begin{aligned} \frac{\partial \mathbf{M}}{\partial \beta} &= -Q\Lambda[\sigma \mathbf{I} + \beta \Lambda]^{-2}Q^T, \\ \frac{\partial \mathbf{M}}{\partial \sigma} &= -Q[\sigma \mathbf{I} + \beta \Lambda]^{-2}Q^T. \end{aligned} \quad (21)$$

The required gradients can then be computed as follows:

$$\begin{aligned} \frac{\partial f}{\partial \beta} &= -L\Delta t x_0 + \frac{\partial \mathbf{M}}{\partial \beta} [\sigma \mathbf{I} \Delta t + \beta L \Delta t (\mathbf{I} + \sigma \mathbf{I} t_0)] \alpha + \mathbf{M} L \Delta t (\mathbf{I} + \sigma \mathbf{I} t_0) \alpha, \\ \frac{\partial f}{\partial \sigma} &= \frac{\partial \mathbf{M}}{\partial \sigma} [\sigma \mathbf{I} \Delta t + \beta L \Delta t (\mathbf{I} + \sigma \mathbf{I} t_0)] \alpha + \mathbf{M} [\mathbf{I} \Delta t + \beta L \Delta t t_0] \alpha, \\ \nabla_\alpha f &= \mathbf{M} [\sigma \mathbf{I} \Delta t + \beta L \Delta t (\mathbf{I} + \sigma \mathbf{I} t_0)] - \mathbf{I} \Delta t. \end{aligned} \quad (22)$$

References

- Adams, J.N., Maass, A., Harrison, T.M., Baker, S.L., Jagust, W.J., 2019. Cortical tau deposition follows patterns of entorhinal functional connectivity in aging. *Elife* 8, e49132.
- Ahmed, Z., Cooper, J., Murray, T.K., Garn, K., McNaughton, E., Clarke, H., Parhizkar, S., Ward, M.A., Cavallini, A., Jackson, S., Bose, S., Clavaguera, F., Tolnay, M., Lavenir, I., Goedert, M., Hutton, M.L., O'Neill, M.J., 2014. A novel in vivo model of tau propagation with rapid and progressive neurofibrillary tangle pathology: the pattern of spread is determined by connectivity, not proximity. *Acta Neuropathol.* 127 (5), 667–683.
- Bassil, F., Brown, H.J., Pattabhiraman, S., Iwasyk, J.E., Maghames, C.M., Meymand, E.S., Cox, T.O., Riddle, D.M., Zhang, B., Trojanowski, J.Q., Lee, V.M., 2020. Amyloid-beta (A β) plaques promote seeding and spreading of alpha-synuclein and tau in a mouse model of Lewy body disorders with A β pathology. *Neuron* 105 (2), 260–275.
- Bejanin, A., Schonhaut, D.R., La Joie, R., Kramer, J.H., Baker, S.L., Sosa, N., Ayakta, N., Cantwell, A., Janabi, M., Lauriola, M., O'Neil, J.P., Gorno-Tempini, M.L., Miller, Z.A., Rosen, H.J., Miller, B.L., Jagust, W.J., Rabinovici, G.D., 2017. Tau pathology and neurodegeneration contribute to cognitive impairment in Alzheimer's disease. *Brain* 140 (12), 3286–3300.
- Boluda, S., Iba, M., Zhang, B., Raible, K.M., Lee, V.M., Trojanowski, J.Q., 2015. Differential induction and spread of tau pathology in young PS19 tau transgenic mice following intracerebral injections of pathological tau from Alzheimer's disease or corticobasal degeneration brains. *Acta Neuropathol.* 129 (2), 221–237.
- Braak, H., Braak, E., 1991. Neuropathological staging of Alzheimer-related changes. *Acta Neuropathol.* 82 (4), 239–259.
- de Calignon, A., Polydoro, M., Suárez-Calvet, M., William, C., Adamowicz, D.H., Kopeikina, K.J., Pistick, R., Sahara, N., Ashe, K.H., Carlson, G.A., Spire-Jones, T.L., Hyman, B.T., 2012. Propagation of tau pathology in a model of early Alzheimer's disease. *Neuron* 73 (4), 685–697.
- Cho, H., Choi, J.Y., Hwang, M.S., Kim, Y.J., Lee, H.M., Lee, H.S., Lee, J.H., Ryu, Y.H., Lee, M.S., Lyoo, C.H., 2016. In vivo cortical spreading pattern of tau and amyloid in the Alzheimer disease spectrum. *Ann. Neurol.* 80 (2), 247–258.
- Dagley, A., LaPoint, M., Huijbers, W., Hedden, T., McLaren, D.G., Chatwal, J.P., Papp, K.V., Amariglio, R.E., Blacker, D., Rentz, D.M., Johnson, K.A., Sperling, R.A., Schultz, A.P., 2017. Harvard aging brain study: dataset and accessibility. *Neuroimage* 144 (Pt B), 255–258.
- Dale, A.M., Fischl, B., Sereno, M.I., 1999. Cortical surface-based analysis. I. Segmentation and surface reconstruction. *Neuroimage* 9 (2), 179–194.
- DeVos, S.L., Corjuc, B.T., Oakley, D.H., Nobuhara, C.K., Bannon, R.N., Chase, A., Commins, C., Gonzalez, J.A., Dooley, P.M., Frosch, M.P., Hyman, B.T., 2018. Synaptic tau seeding precedes tau pathology in human Alzheimer's disease brain. *Front. Neurosci.* 12, 267.
- Donohue, M.C., Sperling, R.A., Petersen, R., Sun, C.K., Weiner, M.W., Aisen, P.S., 2017. Association between elevated brain amyloid and subsequent cognitive decline among cognitively normal persons. *JAMA* 317 (22), 2305–2316.
- Dubois, B., Hampel, H., Feldman, H.H., Scheltens, P., Aisen, P., Andrieu, S., Bakardjian, H., Benali, H., Bertram, L., Blennow, K., Broich, K., Cavado, E., Crutch, S., Dartigues, J.F., Duyckaerts, C., Epelbaum, S., Frisoni, G.B., Gauthier, S., Genthon, R., Gouw, A.A., Habert, M.O., Holtzman, D.M., Kivipelto, M., Lista, S., Molinuevo, J.L., O'Bryant, S.E., Rabinovici, G.D., Rowe, C., Salloway, S., Schneider, L.S., Sperling, R., Teichmann, M., Carrillo, M.C., Cummings, J., Jack, C.R., 2016. Preclinical Alzheimer's disease: definition, natural history, and diagnostic criteria. *Alzheimers Dement* 12 (3), 292–323.
- Fischl, B., Sereno, M.I., Dale, A.M., 1999. Cortical surface-based analysis. II: inflation, flattening, and a surface-based coordinate system. *Neuroimage* 9 (2), 195–207.
- Franzmeier, N., Dewenter, A., Frontzkowski, L., Dichgans, M., Rubinski, A., Neitzel, J., Smith, R., Strandberg, O., Ossenkoppele, R., Buerger, K., Duering, M., Hansson, O., Ewers, M., 2020. Patient-centered connectivity-based prediction of tau pathology spread in Alzheimer's disease. *Sci. Adv.* 6 (48), eabd1327.
- Franzmeier, N., Rubinski, A., Neitzel, J., Kim, Y., Damm, A., Na, D.L., Kim, H.J., Lyoo, C.H., Cho, H., Finsterwalder, S., Duering, M., Seo, S.W., Ewers, M., 2019. Functional connectivity associated with tau levels in ageing, Alzheimer's, and small vessel disease. *Brain* 142 (4), 1093–1107.
- Frost, B., Diamond, M.I., 2010. Prion-like mechanisms in neurodegenerative diseases. *Nat. Rev. Neurosci.* 11 (3), 155–159.
- Garbarino, S., Lorenzi, M., 2019. Modeling and inference of spatio-temporal protein dynamics across brain networks. *Inf. Process. Med. Imaging* 11492, 57–69.
- Girard, G., Caminiti, R., Battaglia-Mayer, A., St-Onge, E., Ambrosen, K.S., Eskildsen, S.F., Krug, K., Dyrby, T.B., Descoteaux, M., Thiran, J.P., Innocenti, G.M., 2020. On the cortical connectivity in the macaque brain: a comparison of diffusion tractography and histological tracing data. *Neuroimage* 221, 117201.
- Gordon, B.A., McCullough, A., Mishra, S., Blazey, T.M., Su, Y., Christensen, J., Dincer, A., Jackson, K., Hornbeck, R.C., Morris, J.C., Ances, B.M., Benzinger, T.L.S., 2018. Cross-sectional and longitudinal atrophy is preferentially associated with tau rather than amyloid positron emission tomography pathology. *Alzheimers Dement (Amst)* 10, 245–252.
- Hanseu, B.J., Betensky, R.A., Jacobs, H.I.L., Schultz, A.P., Sepulcre, J., Becker, J.A., Cosio, D.M.O., Farrell, M., Quiroz, Y.T., Mormino, E.C., Buckley, R.F., Papp, K.V., Amariglio, R.A., Dewachter, I., Ivanov, A., Huijbers, W., Hedden, T., Marshall, G.A., Chhatwal, J.P., Rentz, D.M., Sperling, R.A., Johnson, K., 2019. Association of amyloid and tau with cognition in preclinical Alzheimer disease: a longitudinal study. *JAMA Neurol* 76 (8), 915–924.
- Harrison, T.M., La Joie, R., Maass, A., Baker, S.L., Swinnerton, K., Fenton, L., Mellinger, T.J., Edwards, L., Pham, J., Miller, B.L., Rabinovici, G.D., Jagust, W.J., 2019. Longitudinal tau accumulation and atrophy in aging and Alzheimer disease. *Ann. Neurol.* 85 (2), 229–240.
- Hauglund, N.L., Pavan, C., Nedergaard, M., 2020. Cleaning the sleeping brain – the potential restorative function of the glymphatic system. *Curr. Opin. Physiol.* 15, 1–6.

- He, Z., Guo, J.L., McBride, J.D., Narasimhan, S., Kim, H., Changolkar, L., Zhang, B., Gathagan, R.J., Yue, C., Dengler, C., Stieber, A., Nitla, M., Coulter, D.A., Abel, T., Brun- den, K.R., Trojanowski, J.Q., Lee, V.M., 2018. Amyloid- β plaques enhance Alzheimer's brain tau-seeded pathologies by facilitating neuritic plaque tau aggregation. *Nat. Med.* 24 (1), 29–38.
- Hebert, L.E., Weuve, J., Scherr, P.A., Evans, D.A., 2013. Alzheimer disease in the United States (2010–2050) estimated using the 2010 census. *Neurology* 80 (19), 1778–1783.
- Hedden, T., Oh, H., Younger, A.P., Patel, T.A., 2013. Meta-analysis of amyloid-cognition relations in cognitively normal older adults. *Neurology* 80 (14), 1341–1348.
- Herholz, K., Ebmeier, K., 2011. Clinical amyloid imaging in Alzheimer's disease. *Lancet Neurol* 10 (7), 667–670.
- Holmes, B.B., Furman, J.L., Mahan, T.E., Yamasaki, T.R., Mirbaha, H., Eades, W.C., Bellaygorod, L., Cairns, N.J., Holtzman, D.M., Diamond, M.I., 2014. Proteopathic tau seeding predicts tauopathy in vivo. *Proc. Natl. Acad. Sci. USA* 111 (41), E4376–4385.
- Hu, C., Hua, X., Ying, J., Thompson, P.M., Fakhri, G.E., Li, Q., 2016. Localizing sources of brain disease progression with network diffusion model. *IEEE J. Sel. Top. Signal Process.* 10 (7), 1214–1225.
- Hytinen, J.M., Amadio, M., Viiri, J., Pascale, A., Salminen, A., Kaarniranta, K., 2014. Clearance of misfolded and aggregated proteins by aggregophagy and implications for aggregation diseases. *Ageing Res. Rev.* 18, 16–28.
- Iturria-Medina, Y., Sotero, R.C., Toussaint, P.J., Evans, A.C., Alzheimer's Disease Neuroimaging Initiative, 2014. Epidemic spreading model to characterize misfolded proteins propagation in aging and associated neurodegenerative disorders. *PLoS Comput. Biol.* 10 (11), e1003956.
- Jack, C.R., Barrio, J.R., Kepe, V., 2013. Cerebral amyloid PET imaging in Alzheimer's disease. *Acta Neuropathol.* 126 (5), 643–657.
- Jack, C.R., Bennett, D.A., Blennow, K., Carrillo, M.C., Dunn, B., Haeberlein, S.B., Holtzman, D.M., Jagust, W., Jessen, F., Karlawish, J., Liu, E., Molinuevo, J.L., Montine, T., Phelps, C., Rankin, K.P., Rowe, C.C., Scheltens, P., Siemers, E., Snyder, H.M., Sperling, R., Elliott, C., Masliah, E., Ryan, L., Silverberg, N., 2018. NIA-AA research framework: toward a biological definition of Alzheimer's disease. *Alzheimers Dement* 14 (4), 535–562.
- Jack, C.R., Knopman, D.S., Jagust, W.J., Shaw, L.M., Aisen, P.S., Weiner, M.W., Petersen, R.C., Trojanowski, J.Q., 2010. Hypothetical model of dynamic biomarkers of the Alzheimer's pathological cascade. *Lancet Neurol* 9 (1), 119–128.
- Jack, C.R., Wiste, H.J., Schwarz, C.G., Lowe, V.J., Senjem, M.L., Vemuri, P., Weigand, S.D., Therneau, T.M., Knopman, D.S., Gunter, J.L., Jones, D.T., Graff-Radford, J., Kantarci, K., Roberts, R.O., Mielke, M.M., Machulda, M.M., Petersen, R.C., 2018. Longitudinal tau PET in ageing and Alzheimer's disease. *Brain* 141 (5), 1517–1528.
- Jacobs, H.I.L., Hedden, T., Schultz, A.P., Sepulcre, J., Perea, R.D., Amariglio, R.E., Papp, K.V., Rentz, D.M., Sperling, R.A., Johnson, K.A., 2018. Structural tract alterations predict downstream tau accumulation in amyloid-positive older individuals. *Nat. Neurosci.* 21 (3), 424–431.
- Jenkinson, M., Beckmann, C.F., Behrens, T.E., Woolrich, M.W., Smith, S.M., 2012. FSL. *Neuroimage* 62 (2), 782–790.
- Johnson, K.A., Schultz, A., Betensky, R.A., Becker, J.A., Sepulcre, J., Rentz, D., Mormino, E., Chhatwal, J., Amariglio, R., Papp, K., Marshall, G., Albers, M., Mauro, S., Pepin, L., Alverio, J., Judge, K., Philiosaint, M., Shoup, T., Yokell, D., Dickerson, B., Gomez-Isla, T., Hyman, B., Vasdev, N., Sperling, R., 2016. Tau positron emission tomographic imaging in aging and early Alzheimer disease. *Ann. Neurol.* 79 (1), 110–119.
- Kaufman, S.K., Del Tredici, K., Thomas, T.L., Braak, H., Diamond, M.I., 2018. Tau seeding activity begins in the transentorhinal/entorhinal regions and anticipates phospho-tau pathology in Alzheimer's disease and PART. *Acta Neuropathol.* 136 (1), 57–67.
- Kim, H.R., Lee, P., Seo, S.W., Roh, J.H., Oh, M., Oh, J.S., Oh, S.J., Kim, J.S., Jeong, Y., 2019. Comparison of amyloid $A\beta$ and tau spread models in Alzheimer's disease. *Cereb. Cortex* 29 (10), 4291–4302.
- La Joie, R., Visani, A.V., Baker, S.L., Brown, J.A., Bourakova, V., Cha, J., Chaudhry, D., Edwards, L., Iaccarino, L., Iaccarino, L., Janabi, M., Lesman-Segev, O.H., Miller, Z.A., Perry, D.C., O'Neil, J.P., Pham, J., Rojas, J.C., Rosen, H.J., Seeley, W.W., Tsai, R.M., Miller, B.L., Jagust, W.J., Rabinovici, G.D., 2020. Prospective longitudinal atrophy in Alzheimer's disease correlates with the intensity and topography of baseline tau-PET. *Sci. Transl. Med.* 12 (524), eaa5732.
- Lee, M.J., Lee, J.H., Rubinsztein, D.C., 2013. Tau degradation: the ubiquitin-proteasome system versus the autophagy-lysosome system. *Prog. Neurobiol.* 105, 49–59.
- Lee, S.J., Desplats, P., Sigurdson, C., Tsigelny, I., Masliah, E., 2010. Cell-to-cell transmission of non-prion protein aggregates. *Nat. Rev. Neurosci.* 6 (12), 702–706.
- de Leon, M.J., Blennow, K., 2018. Therapeutic potential for peripheral clearance of misfolded brain proteins. *Nat. Rev. Neurosci.* 14 (11), 637–638.
- Lois, C., Gonzalez, I., Johnson, K.A., Price, J.C., 2019. PET imaging of tau protein targets: a methodology perspective. *Brain Imaging Behav.* 13 (2), 333–344.
- Marque, M., Siao Tick Chong, M., Anton-Fernandez, A., Verwer, E.E., Saez-Calveras, N., Meltzer, A.C., Ramanan, P., Amaral, A.C., Gonzalez, J., Normandin, M.D., Frotscher, M.P., Gomez-Isla, T., 2017. [F-18]-AV-1451 binding correlates with post-mortem neurofibrillary tangle Braak staging. *Acta Neuropathol.* 134 (4), 619–628.
- Nussbaum, J.M., Schilling, S., Cynis, H., Silva, A., Swanson, E., Wangsanut, T., Taylor, K., Wiltgen, B., Hatami, A., Ronicke, R., Reymann, K., Hutter-Paier, B., Alexandru, A., Jagla, W., Graubner, S., Glabe, C.G., Demuth, H.U., Bloom, G.S., 2012. Prion-like behaviour and tau-dependent cytotoxicity of pyroglutamylated amyloid- β . *Nature* 485 (7400), 651–655.
- Nussbaum, J.M., Seward, M.E., Bloom, G.S., 2013. Alzheimer disease: a tale of two prions. *Prion* 7 (1), 14–19.
- Ossenkoppele, R., Schonhaut, D.R., Schöll, M., Lockhart, S.N., Ayakta, N., Baker, S.L., O'Neil, J.P., Janabi, M., Lazaris, A., Cantwell, A., Vogel, J., Santos, M., Miller, Z.A., Bettscher, B.M., Vessel, K.A., Kramer, J.H., Gorno-Tempini, M.L., Miller, B.L., Jagust, W.J., Rabinovici, G.D., 2016. Tau PET patterns mirror clinical and neuroanatomical variability in Alzheimer's disease. *Brain* 139 (Pt 5), 1551–1567.
- Palmqvist, S., Schöll, M., Strandberg, O., Mattsson, N., Stomrud, E., Zetterberg, H., Blennow, K., Landau, S., Jagust, W., Hansson, O., 2017. Earliest accumulation of -amyloid occurs within the default-mode network and concurrently affects brain connectivity. *Nat. Commun.* 8 (1), 1214.
- Raj, A., Kuceyeski, A., Weiner, M., 2012. A network diffusion model of disease progression in dementia. *Neuron* 73 (6), 1204–1215.
- Raj, A., LoCastro, E., Kuceyeski, A., Tosun, D., Relkin, N., Weiner, M., 2015. Network diffusion model of progression predicts longitudinal patterns of atrophy and metabolism in Alzheimer's disease. *Cell Rep.* 10 (3), 359–369.
- Saint-Aubert, L., Lemoine, L., Chiotis, K., Leuzy, A., Rodriguez-Vieitez, E., Nordberg, A., 2017. Tau PET imaging: present and future directions. *Mol. Neurodegener* 12 (1), 19.
- Sanchez, J.S., Becker, J.A., Jacobs, H.I.L., Hanseeuw, B.J., Jiang, S., Schultz, A.P., Propser, M.J., Katz, S.R., Beiser, A., Satizabal, C.L., O'Donnell, A., DeCarli, C., Killiany, R., El Fakhri, G., Normandin, M.D., Gomez-Isla, T., Quiroz, Y.T., Rentz, D.M., Sperling, R.A., Seshadri, S., Augustinack, J., Price, J.C., Johnson, K.A., 2021. The cortical origin and initial spread of medial temporal tauopathy in Alzheimer's disease assessed with positron emission tomography. *Sci. Transl. Med.* 13 (577), eabc0655.
- Scholl, M., Lockhart, S.N., Schonhaut, D.R., O'Neil, J.P., Janabi, M., Ossenkoppele, R., Baker, S.L., Vogel, J.W., Faria, J., Schwimmer, H.D., Rabinovici, G.D., Jagust, W.J., 2016. PET imaging of tau deposition in the aging human brain. *Neuron* 89 (5), 971–982.
- Schwarz, A.J., Shcherbinin, S., Sliker, L.J., Risacher, S.L., Charil, A., Irizarry, M.C., Fleisher, A.S., Southeal, S., Joshi, A.D., Devous, M.D., Miller, B.B., Saykin, A.J., 2018. Topographic staging of tau positron emission tomography images. *Alzheimers Dement (Amst)* 10, 221–231.
- Schwarz, A.J., Yu, P., Miller, B.B., Shcherbinin, S., Dickson, J., Navitsky, M., Joshi, A.D., Devous, M.D., Mintun, M.S., 2016. Regional profiles of the candidate tau PET ligand ^{18}F -Flortaucipir -AV-1451 recapitulate key features of Braak histopathological stages. *Brain* 139 (Pt 5), 1539–1550.
- Sepulcre, J., Grothe, M.J., Sabuncu, M., Chhatwal, J., Schultz, A.P., Hanseeuw, B., El Fakhri, G., Sperling, R., Johnson, K.A., 2017. Hierarchical organization of tau and amyloid deposits in the cerebral cortex. *JAMA Neurol* 74 (7), 813–820.
- Sepulcre, J., Grothe, M.J., Quillas, F., Ortiz-Teran, L., Diez, I., Yang, H.-S., Jacobs, H., Hanseeuw, B., Li, Q., El Fakhri, G., Sperling, R., Johnson, K.A., 2008. Neurogenetic contributions to amyloid beta and tau spreading in the human cortex. *Nat. Med.* 24 (12), 1910–1918.
- Sepulcre, J., Schultz, A.P., Sabuncu, M., Gomez-Isla, T., Chhatwal, J., Becker, A., Sperling, R., Johnson, K.A., 2016. In vivo tau, amyloid, and gray matter profiles in the aging brain. *J. Neurosci.* 36 (28), 7364–7374.
- Shafiei, S.S., Guerrero-Munoz, M.J., Castillo-Carranza, D.L., 2017. Tau oligomers: cytotoxicity, propagation, and mitochondrial damage. *Front. Aging Neurosci.* 9, 83.
- Smith, S.M., Jenkinson, M., Woolrich, M.W., Beckmann, C.F., Behrens, T.E., Johansen-Berg, H., Bannister, P.R., De Luca, M., Drobnjak, I., Flitney, D.E., Niazy, R.K., Saunders, J., Vickers, J., Zhang, Y., De Stefano, N., Brady, J.M., Matthews, P.M., 2004. Advances in functional and structural MR image analysis and implementation as FSL. *Neuroimage* 23 (Suppl 1), S208–219.
- Song, T.-A., Yang, F., Chowdhury, S., Kim, K., Johnson, K., El Fakhri, G., Li, Q., Dutta, J., 2019. PET image deblurring and super-resolution with an MR-based joint entropy prior. *IEEE Trans. Comput. Imaging* 5 (4), 530–539.
- Sperling, R., Mormino, E., Johnson, K., 2014. The evolution of preclinical Alzheimer's disease: implications for prevention trials. *Neuron* 84 (3), 608–622.
- Sperling, R.A., Aisen, P.S., Beckett, L.A., Bennett, D.A., Craft, S., Fagan, A.M., Iwatsubo, T., Jack, C.R., Kaye, J., Montine, T.J., Park, D.C., Reiman, E.M., Rowe, C.C., Siemers, E., Stern, Y., Yaffe, K., Carrillo, M.C., Thies, B., Morrison-Bogorad, M., Wagster, M.V., Phelps, C.H., 2011. Toward defining the preclinical stages of Alzheimer's disease: recommendations from the national institute on aging-Alzheimer's association workgroups on diagnostic guidelines for Alzheimer's disease. *Alzheimers Dement* 7 (3), 280–292.
- Strain, J.F., Smith, R.X., Beaumont, H., Roe, C.M., Gordon, B.A., Mishra, S., Adeyemo, B., Christensen, J.J., Su, Y., Morris, J.C., Benzinger, T.L.S., Ances, B.M., 2018. Loss of white matter integrity reflects tau accumulation in Alzheimer disease defined regions. *Neurology* 91 (4), e313–e318.
- Torok, J., Maia, P.D., Powell, F., Pandya, S., Raj, A., 2018. A method for inferring regional origins of neurodegeneration. *Brain* 141 (3), 863–876.
- Vogel, J.W., Iturria-Medina, Y., Strandberg, O.T., Smith, R., Levitis, E., Evans, A.C., Hansson, O., Alzheimer's Disease Neuroimaging Initiative, Swedish BioFinder Study, 2020. Spread of pathological tau proteins through communicating neurons in human Alzheimer's disease. *Nat. Commun.* 11 (1), 1–15.
- Woo, J.A., Liu, T., Fang, C.C., Castañón, M.A., Kee, T., Yrigoin, K., Yan, Y., Cazzaro, S., Matlack, J., Wang, X., Zhao, X., Kang, D.E., Liggett, S.B., 2020. β -Arrestin2 oligomers impair the clearance of pathological tau and increase tau aggregates. *Proc. Natl. Acad. Sci. USA* 117 (9), 5006–5015.
- Woolrich, M.W., Jbabdi, S., Patenaude, B., Chappell, M., Makni, S., Behrens, T., Beckmann, C., Jenkinson, M., Smith, S.M., 2009. Bayesian analysis of neuroimaging data in FSL. *Neuroimage* 45 (1 Suppl), S173–186.
- Xia, C., Makarets, S.J., Caso, C., McGinnis, S., Gomperts, S.N., Sepulcre, J., Gomez-Isla, T., Hyman, B.T., Schultz, A., Vasdev, N., Johnson, K.A., Dickerson, B.C., 2017. Association of in vivo [^{18}F]-Flortaucipir [AV-1451] tau PET imaging results with cortical atrophy and symptoms in typical and atypical Alzheimer disease. *JAMA Neurol* 74 (4), 427–436.
- Yang, F., Chowdhury, S.R., Jacobs, H.I.L., Johnson, K.A., Dutta, J., 2019. A longitudinal model for tau aggregation in Alzheimer's disease based on structural connectivity. *Inf. Process. Med. Imaging* 11492, 384–393.